applied sciences

MDPI

Article

Experimental Investigation of the Mechanical Performance of Steel Fiber-Reinforced Concrete Tunnel Linings Under Freeze–Thaw Cycles

Li-Ming Wu [1,2], Feng Gao [1], Zi-Jian Wang [3,*], Lan-Shen Li [3,*], Hu-Xin-Tong Huang [3] and Wen-Jie Luo [3]

[1] School of Civil Engineering, Chongqing Jiaotong University, Chongqing 400074, China; wulm@cqtbi.edu.cn (L.-M.W.); gaofeng1964@163.com (F.G.)
[2] School of Urban Construction Engineering, Chongqing Technology and Business Institute, Chongqing 400052, China
[3] School of Civil and Hydraulic Engineering, Chongqing University of Science and Technology, Chongqing 401331, China; 2023206011@cqust.edu.cn (W.-J.L.)
* Correspondence: 2013016@cqust.edu.cn (Z.-J.W.); 2024206001@cqust.edu.cn (L.-S.L.)

Abstract

Tunnel lining models were cast at a 1:20 scale using four different materials: plain concrete (PC), steel fiber-reinforced concrete (SFRC), reinforced concrete (RC), and rebar-reinforced steel fiber-reinforced concrete (R/SFRC). Loading tests were performed on these models before and after freeze–thaw cycles to investigate the failure modes, analyze the mechanical behavior, and determine the optimal reinforcement scheme in this study. The results indicated that freeze–thaw cycling reduced the load-bearing capacity of tunnel linings by 12% to 28% compared to non-freeze–thaw linings. Adding steel fibers significantly enhanced the ductility of the lining models. The mechanical performance of linings with an optimal steel fiber content surpassed that of models with either increased rebar alone or steel fibers alone. In this study, an optimal combination of a 0.36% rebar ratio and a 1.5% steel fiber volume fraction effectively improved the tensile performance of the lining while reducing rebar consumption, without compromising the inherent mechanical performance of the tunnel structure.

Keywords: freeze–thaw cycles; steel fiber-reinforced concrete (SFRC); mechanical behavior; scaled model

1. Introduction

Driven by rapid economic development and national strategies such as the "Belt and Road" Initiative and the "Yangtze River Economic Belt," tunnel construction in colder regions of China has seen a significant increase in both number and scale. This expansion, however, presents substantial engineering challenges. A primary concern is the deterioration of concrete caused by freeze–thaw cycles, which is major reason for failure in colder climates [1,2]. Concrete with inadequate durability suffers progressive microstructural damage under repeated freezing and thawing, leading to reduced service life, increased maintenance costs, and compromised economic viability [3].

To address performance degradation and structural failure in tunnels under freeze–thaw action, researchers have conducted extensive studies. Experimental work has focused on strength deterioration patterns [4] and the failure modes of lining structures [5], while numerical simulations have been employed to analyze the service performance evolution of linings under such conditions [6].

Check for updates

Academic Editor: Sebastiano Candamano

Received: 3 February 2026
Revised: 5 March 2026
Accepted: 23 March 2026
Published: 26 March 2026

Copyright: © 2026 by the authors. Licensee MDPI, Basel, Switzerland. This article is an open access article distributed under the terms and conditions of the Creative Commons Attribution (CC BY) license.

Concurrently, the development of advanced materials offers potential solutions. Among these, steel fiber-reinforced concrete (SFRC) has attracted significant interest for performance enhancement [7–9]. Research indicates that freeze–thaw cycles damage the internal structure of SFRC, affecting its stress–strain response [10] and leading to quantifiable damage evolution, which can be modeled effectively [11].

As the number of freeze–thaw cycles increases, plain concrete develops a crack network with a loosened microstructure. In contrast, the incorporation of steel fibers restricts crack propagation, demonstrating a pronounced strengthening and crack-resisting effect. Ref. [12] enhanced properties such as splitting tensile strength and frost durability life [13]. Notably, the mitigating effect of fibers on freeze–thaw damage is content-dependent; higher fiber dosages better preserve dynamic tensile performance [14] and reduce crack permeability in damaged concrete [15]. This protective role of steel fibers against performance degradation and durability loss under freeze–thaw cycles has been consistently confirmed [16–18], with demonstrated improvements in mechanical properties [19,20]. Critically, an optimal fiber volume fraction (e.g., 1.5%) has been identified to significantly retard the frost damage deterioration process [21].

While considerable research has been conducted on SFRC under freeze–thaw cycles, critical gaps persist. Specifically, experimental data on the structural response and failure mechanisms of integral tunnel linings in cold regions under combined thermo-mechanical loading are lacking. Furthermore, existing studies on the mechanical and durability properties of SFRC are primarily confined to standard ambient conditions, with insufficient attention to its performance in the extreme composite environment typical of cold regions—characterized by high geostatic stress, sustained low temperatures, and cyclic freeze–thaw action. To address these gaps, this study investigates four lining structure types: PC, RC, SFRC, and R/SFRC. This study elucidates the damage evolution process and failure modes of such linings through scaled model tests, ultimately identifying the optimal hybrid reinforcement configuration that achieves superior structural performance in the proposed design.

2. Construction of Scaled Tunnel Structure Models

2.1. Design of the Tunnel Structure Model Test

This study utilizes a tunnel in Gannan Tibetan Autonomous Prefecture, Gansu Province, as the engineering background. The prototype tunnel is approximately 930 m in total length, corresponding to a medium-length tunnel. The site is characterized by a high-altitude, cold, and humid climate, with an annual average temperature of 4.6 °C. The highest and lowest monthly average temperatures are 14.8 °C (July) and −7.6 °C, respectively, at an altitude of about 3300 m. Guided by the cross-sectional design requirements stipulated in the Specifications for Design of Highway Tunnels, Section 1: Civil Engineering (JTG/T 3370.1-2018) [22], and considering the experimental objectives and constraints, the original lining dimensions were optimized and geometrically scaled. A scaling ratio of 1:20 was applied to the lining thickness, resulting in a model thickness of 40 mm to facilitate casting and compaction. The longitudinal length of the model was set to 80 cm. Figure 1 presents the scaled tunnel model. A dedicated steel mold was fabricated according to the scaled dimensions for casting the lining segments. The mold was constructed from 5 mm thick steel plates. Holes with a diameter of 10 mm were drilled into these plates. The mold had a longitudinal dimension of 800 mm. At each longitudinal end, a 40 mm wide steel plate strip (accounting for the lining thickness) was welded. The holes on these end strips were centered. Schematic diagrams detailing the mold components are provided in Figure 2.

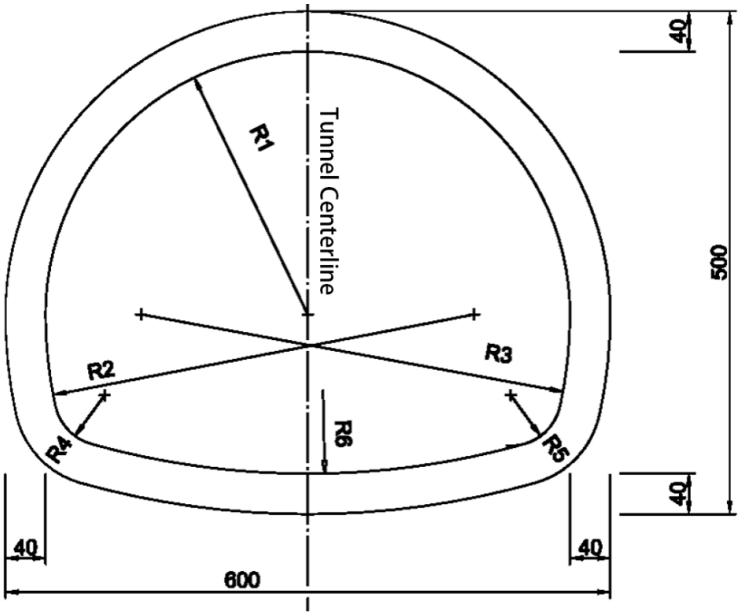


Figure 1. Tunnel cross section (scale 1:20).

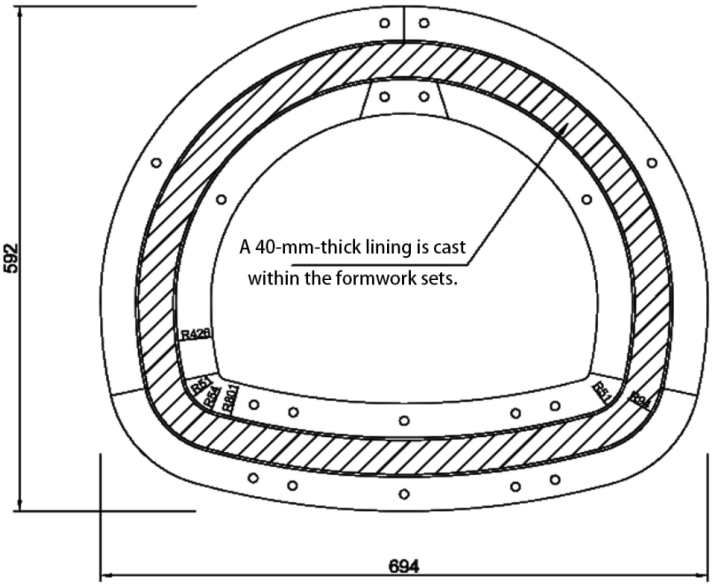


Figure 2. Schematic of the tunnel lining formwork cross-section.

2.2. Casting of Tunnel Models

Tunnel lining models were fabricated on a 1:20 geometric scale. The base concrete matrix comprised 10% silica fume, a water to binder ratio (w/b) of 0.40, and 1% superplasticizer. Steel fibers (1.5% by volume) were added to produce SFRC. Four lining types were cast: (i) PC using the base matrix; (ii) RC, ρ = 0.45% using the base matrix; (iii) SFRC; and (iv) R/SFRC, ρ = 0.36%.

The tunnel lining models were cast following a standardized procedure. The key construction steps comprised formwork erection, installation of steel wire mesh, mixing of concrete (including SFRC variants), internal manual vibration combined with external mechanical vibration of the forms, demolding, and curing. The overall casting process is documented in Figure 3.



(**a**) Assembly of inner steel formwork (**b**) Installation of steel wire mesh

(**c**) Batching of casting materials (**d**) Mixing of materials

(**e**) Manual internal vibration (**f**) Mechanical external vibration of formwork

(**g**) Demolding process of tunnel model (**h**) Completed demolding of tunnel model

Figure 3. Schematic diagram of the complete tunnel model casting process.

2.3. Similitude Relationships and Test Materials

Based on similarity theory, the scaling factors for the physical quantities were calculated and are presented in Table 1. Key parameters, including stiffness, strength, load, and elastic resistance coefficient, all satisfy the similarity requirements. However, due to the complexity of model similitude, the concrete density and steel fiber dimensions deviate from strict similarity theory. Provided that the influence of self-weight is neglected, prototype materials can still be adopted in the model test. This approach ensures that the model test effectively simulates the actual working conditions, accurately reproducing the mechanical behavior and damage characteristics of the concrete lining.

Table 1. Model test materials.

Mineral Admixture	Cementitious Material	Fine Aggregate	Coarse Aggregate	Steel Fiber	Superplasticizer
Silica Fume	Cement	Natural River Sand (fineness modulus: 2.6)	Coarse Aggregate (maximum aggregate size did not exceed 20 mm or two thirds of the steel fiber length)	Milled Steel Fiber (length: 25–35 mm; diameter: 2.45 mm)	Polycarboxylate-Based Superplasticizer

The similitude ratios for key physical parameters, derived from similitude theory, are summarized in Table 2. The listed parameters, including stiffness, strength, applied load, and the coefficient of elastic resistance, all satisfy the established similitude criteria.

Table 2. Similitude ratios of physical parameters for test materials.

Property	Physical Quantity	Unit	Similitude Ratio	Property	Physical Quantity	Unit	Similitude Ratio
Material	Stress	MPa	$C_\sigma = 1$	Geometry and Loading	Dimensions	m	$C_L = 20$
	Young's Modulus	GPa	$C_E = 1$		Displacement	m	$C_\delta = \frac{C_\sigma C_L}{C_E} = 20$
	Density	Kg/m^3	$C_\rho = 1$		Concentrated Force	N	$C_F = C_\sigma C_L^2 = 400$
	Strain	—	$C_\varepsilon = 1$		Bending Moment	N.m	$C_M = C_\sigma C_L^3 = 8000$
	Poisson's Ratio	—	$C_\mu = 1$		Coefficient of Elastic Resistance	N/m^3	$C_k = \frac{C_\sigma}{C_\delta} = 0.05$

Note: Physical quantities for steel fiber materials are actual values.

3. Freeze–Thaw Cycling and Loading Tests on a Tunnel Structure Model

3.1. Freeze–Thaw Cycle Test Design

To investigate the mechanical performance of four tunnel lining types under cold region freeze–thaw cycles, seven scaled models were fabricated. The test series included one PC model (S1), two RC models (S2-1, S2-2), two SFRC models (SF1-1, SF1-2), and two R/SFRC models (SF2-1, SF2-2). The experimental matrix detailing model type, number of freeze–thaw cycles, material composition, and exposure condition is provided in Table 3.

Table 3. Freeze–thaw cycle test matrix for tunnel structure models.

Model Types of Tunnel Structures	Specimen ID	Number of Freeze–Thaw Cycles	Silica Fume Content	SF Volume Fraction	Water Binder Ratio	Reinforcement Ratio	Freeze–Thaw Condition
PC	S1	0	0	0	0.40	0	NO
RC	S2-1	0	0	0	0.40	0.45%	NO
	S2-2	100	0	0	0.40	0.45%	YES
SFRC	SF1-1	0	10%	1.5%	0.40	0	NO
	SF1-2	100	10%	1.5%	0.40	0	YES
R/SFRC	SF2-1	0	10%	1.5%	0.40	0.36%	NO
	SF2-2	100	10%	1.5%	0.40	0.36%	YES

Note: S1: PC. S2: RC with a longitudinal reinforcement ratio of 0.45%, composed of 45 steel wires each with a diameter of 2 mm. SF1: SFRC containing 1.5% steel fibers by volume. SF2: R/SFRC, incorporating 1.5% steel fibers by volume and a longitudinal reinforcement ratio of 0.36% provided by 37 steel wires (2 mm diameter).

Upon completion of curing, the tunnel structural models were subjected to freeze–thaw testing in a temperature/humidity environmental chamber, as specified in Table 3. The chamber features a working volume of 1800 mm (D) × 2500 mm (W) × 1800 mm (H), with a controllable temperature range of −50 °C to +150 °C and a relative humidity range of 20% to 98% RH.

The temperature gradient settings of the climatic test chamber comply with the technical requirements specified in the Standard for Test Methods of Long-Term Performance and Durability of Ordinary Concrete (GB/T 50082-2009) [23]. A corresponding rapid freeze–thaw cycle test protocol was established. Figure 4 presents the temperature time-history curve of multiple freeze–thaw cycles within a 24 h period, along with synchronously monitored temperature variations at the specimen center. One complete cycle was selected for detailed analysis: Figure 5 illustrates the dynamic response between the chamber-controlled temperature and the specimen core temperature during this cycle. To further characterize the temperature gradient, Figure 6 depicts the gradient evolution on the chamber side, while Figure 7 presents the corresponding gradient evolution at the specimen center. The coupled analysis of these Figures reveals the differential thermal response between the chamber control and the internal temperature field of the specimen during freeze–thaw cycling.

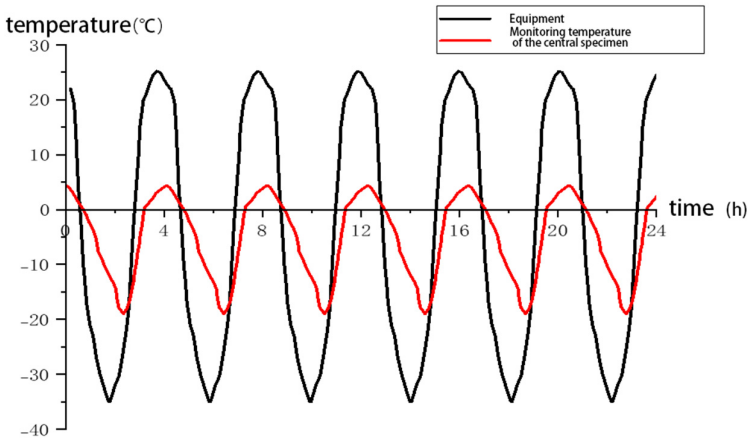


Figure 4. Illustrates the temperature variation in the freeze–thaw apparatus over a 24 h cycle.

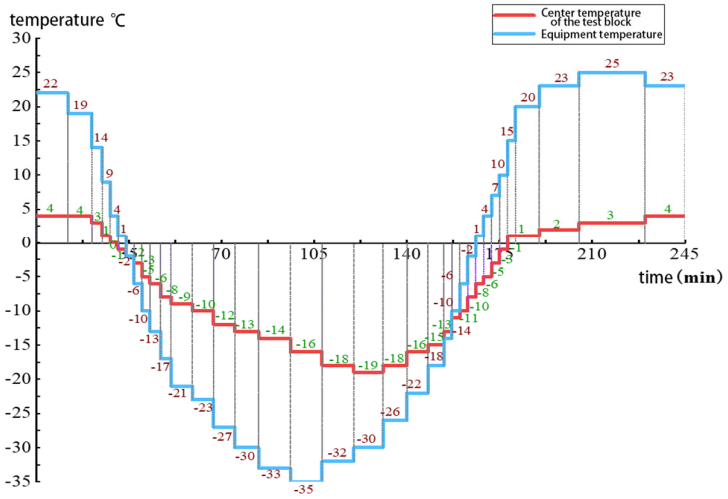


Figure 5. Presents the temperature evolution of the freeze-thaw apparatus and the specimen center over time.

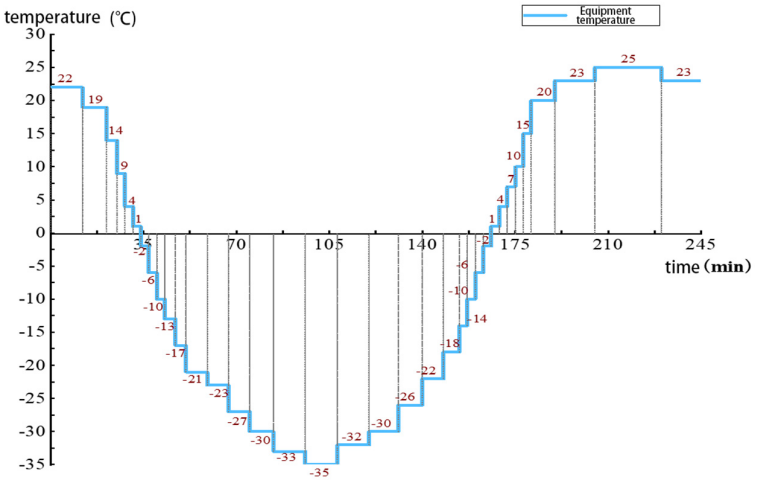


Figure 6. Presents the temperature profile of the freeze-thaw apparatus over one cycle.

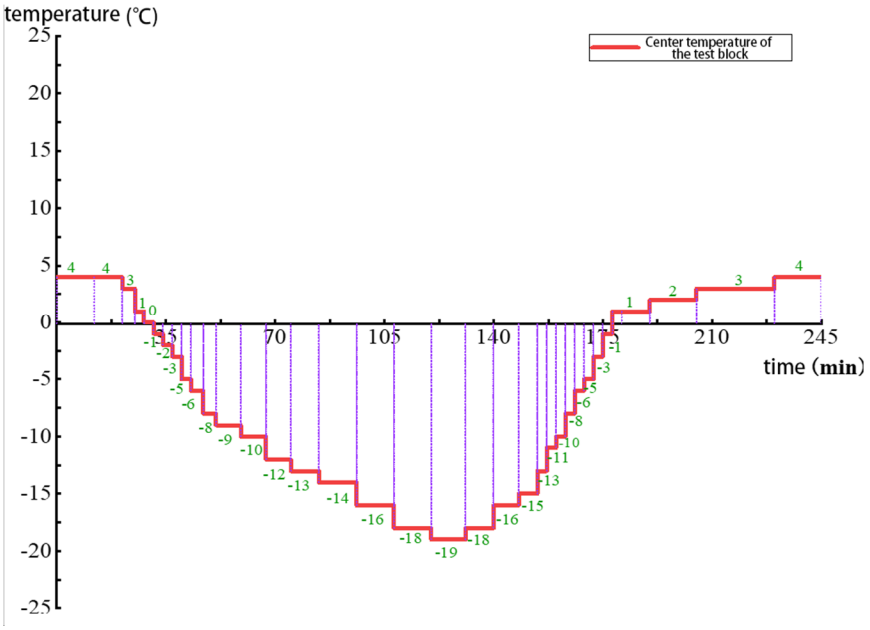


Figure 7. Presents the temperature gradient of the specimen center over one cycle.

3.2. Loading System for Tunnel Models

A reaction frame was adapted as the loading system (Figure 8) to simulate simultaneous vertical and lateral pressures on the lining. The vertical load (simulating overburden) was applied by hydraulic jacks and transferred through steel rods to rigid bearing plates, ensuring a uniform stress distribution. Lateral confining pressure (representing rock mass) was controlled by symmetric servo hydraulic jacks via steel rods.

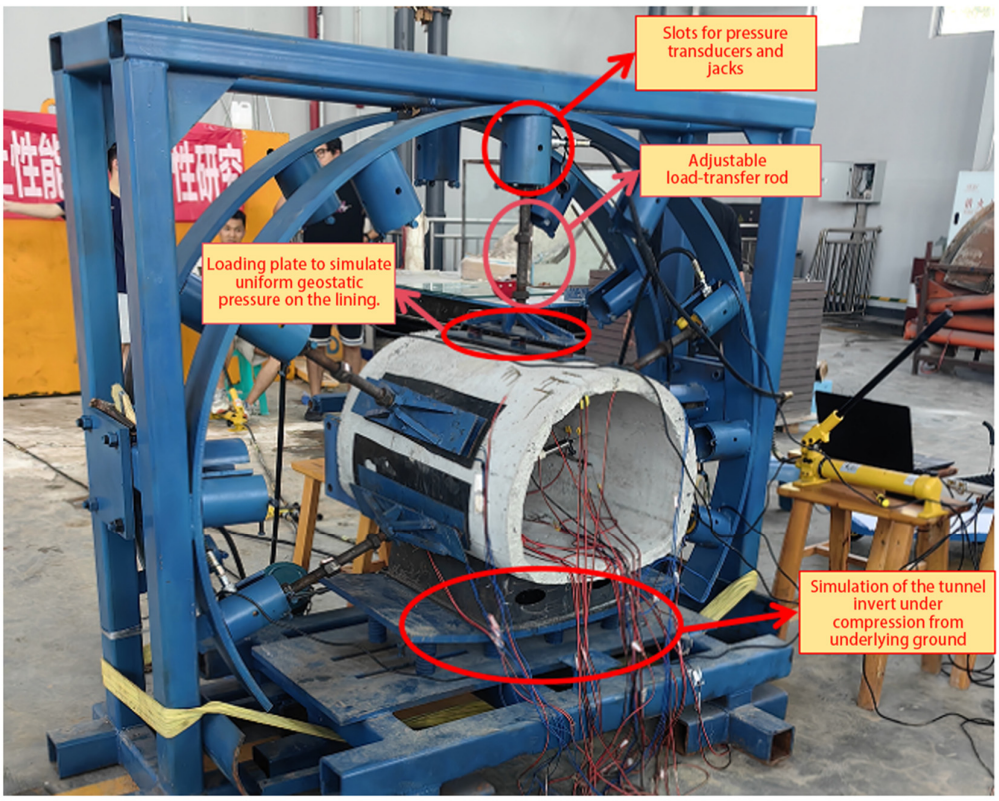


Figure 8. Reaction frame for tunnel lining loading.

This system provided three key capabilities: (1) synchronized biaxial loading via coupled servo control (±0.05 MPa sync precision); (2) real-time, full-field DIC monitoring (50 Hz sampling); and (3) realistic replication of in situ tunnel stress states (validated by stress path similarity >95%).

3.3. Experimental Loading Protocol

A progressive loading technique was employed. The confinement effect of the surrounding rock on the tunnel support system was simulated using load transfer rods installed on both sides of the lining. Bearing plates (50 cm × 10 cm) at the rod lining interfaces ensured uniform load transfer. The load was applied through the top rods and progressively increased to monitor and analyze the mechanical evolution of the four lining systems during progressive failure, with a focus on comparing their failure modes and underlying mechanisms.

A load structure model was applied. The vertical load was applied in increments of 50 kPa. The lateral load increased simultaneously, maintained at a constant ratio of 0.7 times the vertical load to simulate the lateral rock confinement. Each load level was sustained for 1–2 min to allow for the observation of crack initiation and propagation until complete structural failure occurred. This protocol characterized the structural behavior under simulated rock pressure, providing a basis for optimized design.

3.4. Theoretical Background

Kirsch's equation [24] is a commonly used empirical formula for estimating the lateral pressure coefficient K, as given in Equation (1).

$$K = \frac{1 - sin\phi}{1 + sin\phi} \quad (1)$$

Here, ϕ represents the internal friction angle of the surrounding rock. The coefficient of lateral earth pressure (K) typically ranges from 0.4 to 0.7, and was taken as the upper bound value of 0.7 in this test.

4. Analysis of Mechanical Characteristics of Tunnel Lining Structural Models

4.1. Loading Process and Failure Modes of Tunnel Lining Structures

(1) Failure of S1 Tunnel Lining Models

As shown in Figure 9, the test results indicate that instability failure occurred at the 13th loading stage, with a vertical load of 597 kPa. Figure 10 shows the failure state of the S1 tunnel lining model.

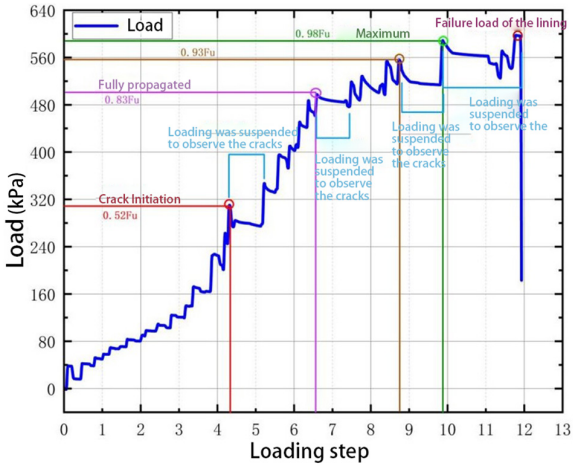


Figure 9. S1 Tunnel lining model loading process.



Figure 10. S1 Tunnel lining model failure state.

(2) Analysis of the Failure Process in S2 Tunnel Lining Models

Figure 11 illustrates the vertical load application process for the S2-1 and S2-2 tunnel lining specimens.

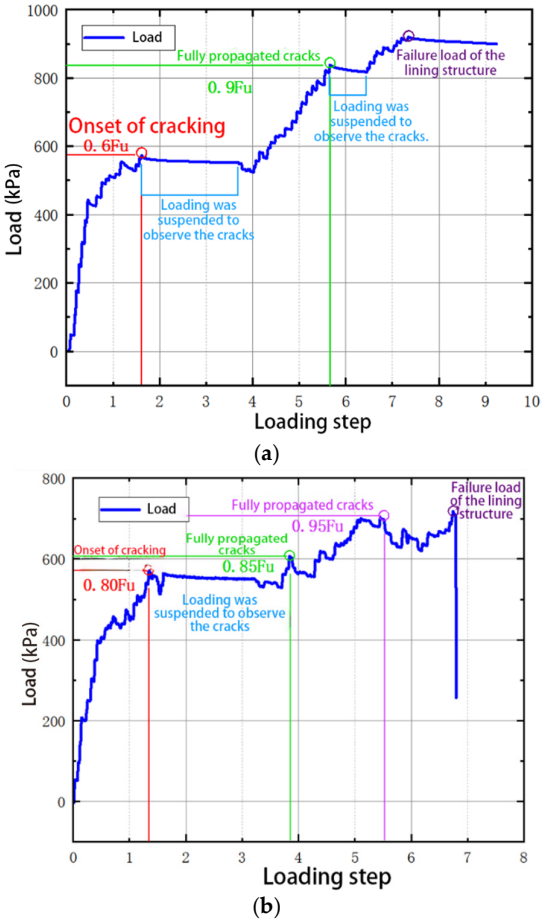


Figure 11. Loading curve of the RC tunnel lining model: (**a**) S2-1 tunnel lining crown; (**b**) S2-2 tunnel lining crown.

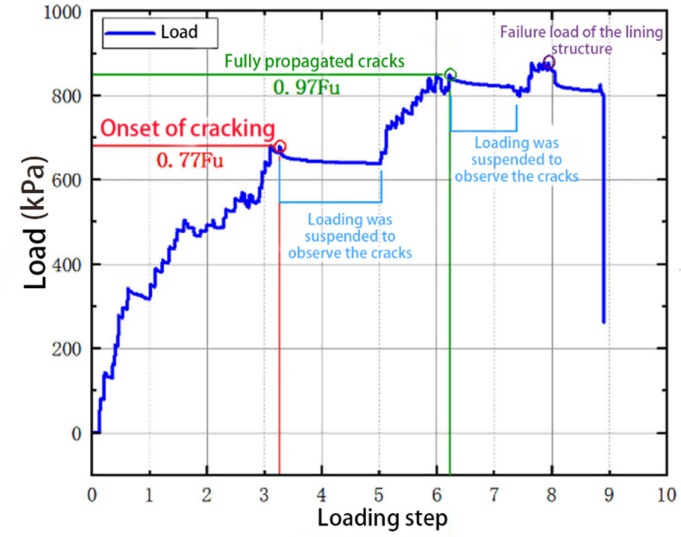
The test data show that specimens S2-1 and S2-2 failed due to instability at the 8th and 7th loading stages (excluding observation pauses), respectively. The corresponding vertical loads at the lining crown were 920 kPa for the unfrozen condition and 718 kPa for the frozen condition. This result indicates a 28% higher bearing capacity in the unfrozen state compared to the frozen condition. Figure 12 shows the final failure pattern of S2-1 and S2-2 tunnel lining models.



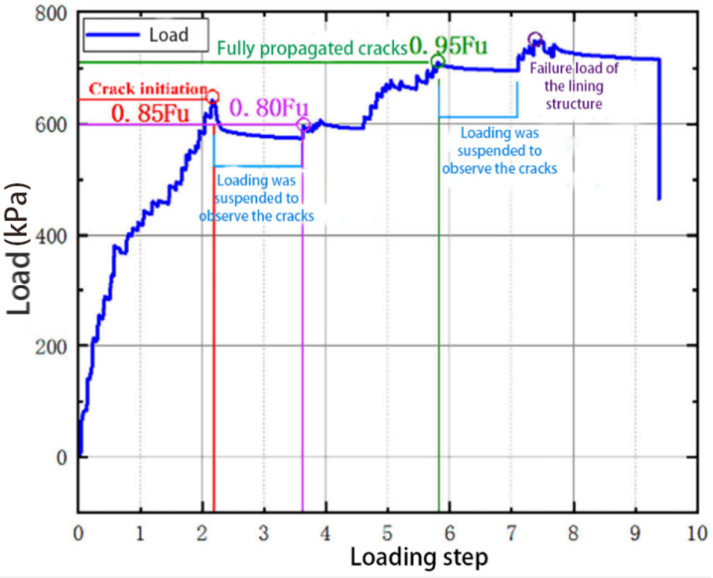
Figure 12. Final failure pattern of S2-1 and S2-2 tunnel lining models.

(3) Analysis of Failure Process in SF1 Tunnel Lining Models

Figure 13 shows the vertical load application process for the SF1-1 and SF1-2 tunnel lining specimens.



(**a**)



(**b**)

Figure 13. Loading curve of the SFRC tunnel lining model: (**a**) SF1-1 tunnel lining crown; (**b**) SF1-2 tunnel lining crown.

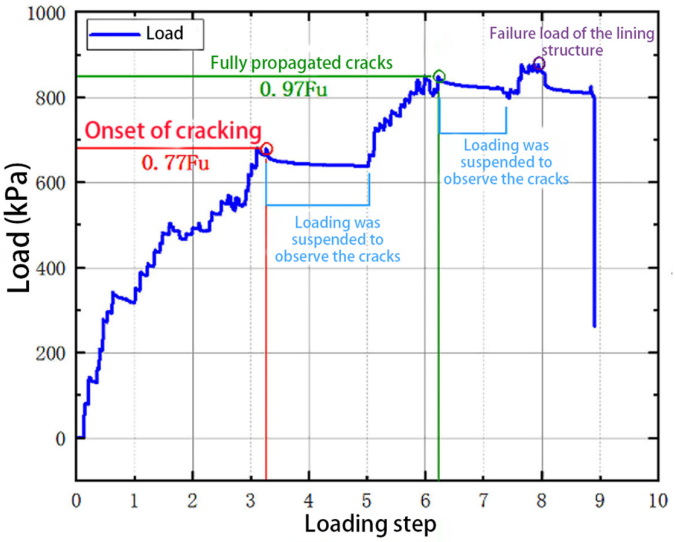
The failure progression of tunnel lining specimens SF1-1 and SF1-2 is detailed in Figure 14. Test data indicate that failure occurred at the 8th loading stage (including observation pauses). At this stage, the vertical crown loads were 876 kPa (unfrozen) and 748 kPa (frozen), corresponding to a 17% higher bearing capacity in the unfrozen condition.

Figure 15 illustrates the vertical load application process for tunnel lining specimens SF2-1 and SF2-2.

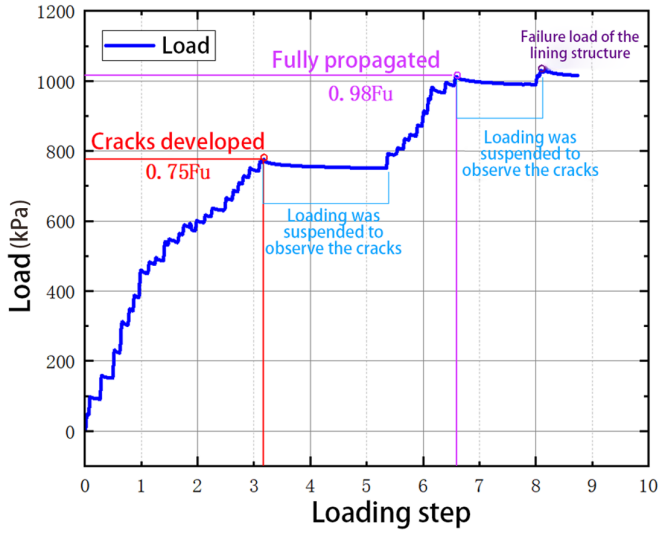


Figure 14. Final failure pattern of SF1-1 and SF1-2 tunnel lining models.

(4) Analysis of Failure Process in SF2 Tunnel Lining Models



(**a**)



(**b**)

Figure 15. Loading curve of the R/SFRC tunnel lining model: (**a**) SF2-1 tunnel lining crown; (**b**) SF2-2 tunnel lining crown.

The failure progression of tunnel lining specimens SF2-1 and SF2-2 is detailed in Figure 15. Test data indicate that the unfrozen specimen failed at the 8th loading stage (including observation pauses), attaining a vertical crown load of 1148 kPa. In comparison, the frozen specimen failed at the 9th loading stage (including observation pauses), reaching a crown load of 1028 kPa—corresponding to a 12% higher bearing capacity for the unfrozen condition. Figure 16 shows the failure mode of tunnel lining models SF2-1 and SF2-2.



Figure 16. Failure mode of tunnel lining models SF2-1 and SF2-2.

For comparative viewing, the post-failure diagrams of the seven tunnel lining structural models are arranged together, as shown in Figure 17.

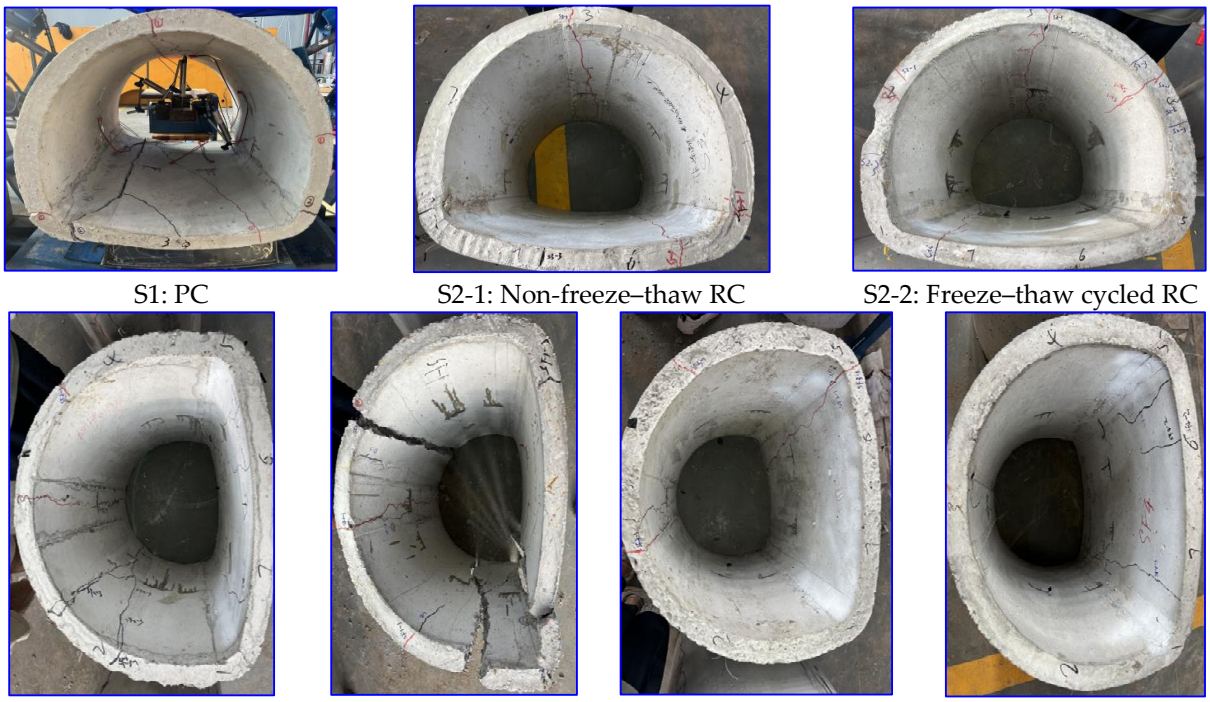


Figure 17. Loading and failure states of the tunnel lining models.

4.2. Comparative Analysis of Lining Models Under Freeze–Thaw and Non-Freeze–Thaw Conditions

1. Bearing Capacity Ranking and Deterioration Pattern: Under non-freeze–thaw conditions, the ultimate bearing capacities of the models rank as SF2-1 > S2-1 > SF1-1 > S1. Following freeze–thaw cycles, this order shifts to SF2-2 > SF1-2 > S2-2 > S1. The results indicate that freeze–thaw action significantly deteriorates the mechanical properties of the structures, leading to a general reduction in bearing capacity and altering the ranking. This underlines the more pronounced weakening effect of freeze–thaw environments on reinforced concrete structures.
2. Comparative Effectiveness of Strengthening: Relative to the PC benchmark, the bearing capacities of models S2-1, SF1-1, and SF2-1 increased by 54%, 47%, and 92%, respectively, under non-freeze–thaw conditions. After freeze–thaw exposure, the corresponding increases for S2-2, SF1-2, and SF2-2 dropped to 20%, 25.3%, and 72.2%. Although the strengthening measures remain effective post-freeze–thaw, their enhancement effect is attenuated. Notably, the most significant reduction in the capacity enhancement rate was observed in the RC structure (S2-2).
3. Comparative Performance of RC vs. SFRC: Under identical reinforcement ratios and steel fiber volume fractions, the bearing capacity of RC exceeds that of SFRC by 5% under non-freeze–thaw conditions, highlighting the strengthening advantage of continuous reinforcement. However, after freeze–thaw cycling, the bearing capacity of SFRC surpasses that of reinforced concrete by 4.2%. This reversal indicates that SFRC not only has the potential to substitute conventional RC but also exhibits superior durability in resisting freeze–thaw deterioration.
4. Model SF2-1 (R/SFRC) exhibits the highest bearing capacity under non-freeze–thaw conditions, demonstrating the additive effect of hybrid reinforcement. Post-freeze–thaw, model SF2-2 retains the highest bearing capacity and a maximum enhancement rate of 72.2%, confirming that incorporating an appropriate amount of steel fibers, even with a reduced reinforcement ratio, not only compensates for capacity loss but also effectively enhances crack resistance and ductility under freeze–thaw exposure.
5. Although SFRC demonstrates superior bearing capacity after freeze–thaw compared to RC, cracks tend to propagate along fiber–matrix interfaces or through weak zones between fibers due to the discontinuous distribution of steel fibers within the matrix. This micro-mechanism fundamentally determines that, despite exhibiting favorable toughness and frost resistance macroscopically, SFRC differs essentially from continuous RC in terms of crack control and structural integrity.

4.3. Structural Analysis of Tunnel Lining Models

Figures 18 and 19 summarize the loading-to-failure behavior of seven tunnel lining models (S1, S2-1, S2-2, SF1-1, SF1-2, SF2-1, and SF2-2), encompassing both non-freeze–thaw and freeze–thaw specimens. The key findings are as follows:

1. The ultimate bearing capacity ranks in the order: SF2-1 > SF2-2 > S2-1 > SF1-1 > SF1-2 > S2-2 > S1.
2. As shown in Figure 19, the percentage increase in bearing capacity relative to the plain concrete (S1) lining follows the sequence: SF2-1 > SF2-2 > S2-1 > SF1-1 > SF1-2 > S2-2. The results indicate a significant reduction in structural capacity due to freeze–thaw action, with reductions of up to 20% observed under identical conditions.
3. The discontinuous distribution of steel fibers forces cracks to propagate through the intervening concrete matrix. Consequently, fracture morphology and failure surfaces reveal that steel fiber-reinforced concrete exhibits brittle failure analogous to plain concrete, with post-freeze–thaw brittleness becoming markedly more pronounced.

Notably, failure in plain steel fiber-reinforced concrete specimens occurs as brittle fracture of the concrete matrix between non-continuous fibers.

4. In the reinforced tunnel lining models, the continuity of the steel reinforcement substantially improved structural ductility under freeze–thaw conditions. Therefore, based on the experimental data from both non-freeze–thaw and freeze–thaw tunnel lining model tests, the optimal structural configuration among the tested models is identified as steel bar and steel fiber-reinforced concrete.

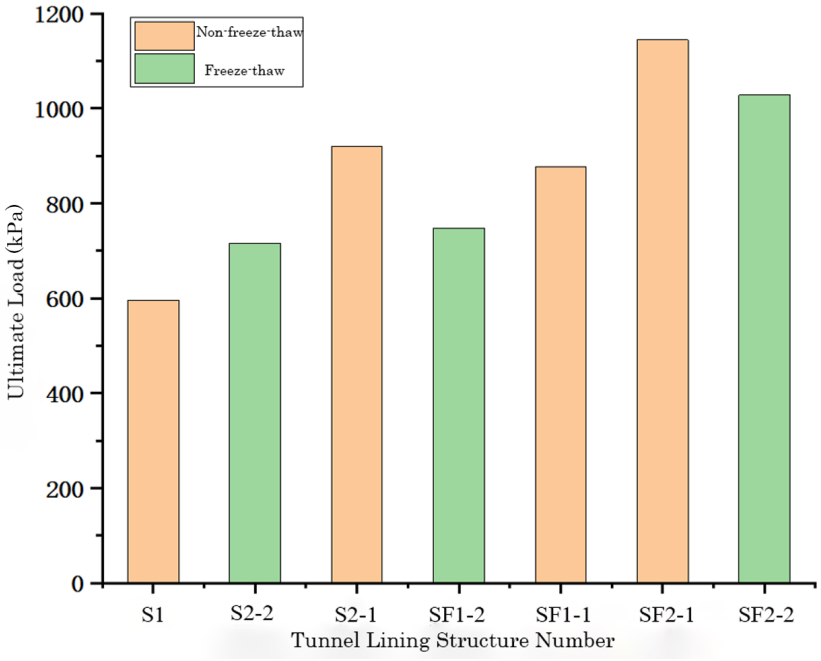


Figure 18. Ultimate load capacity of the tunnel lining.

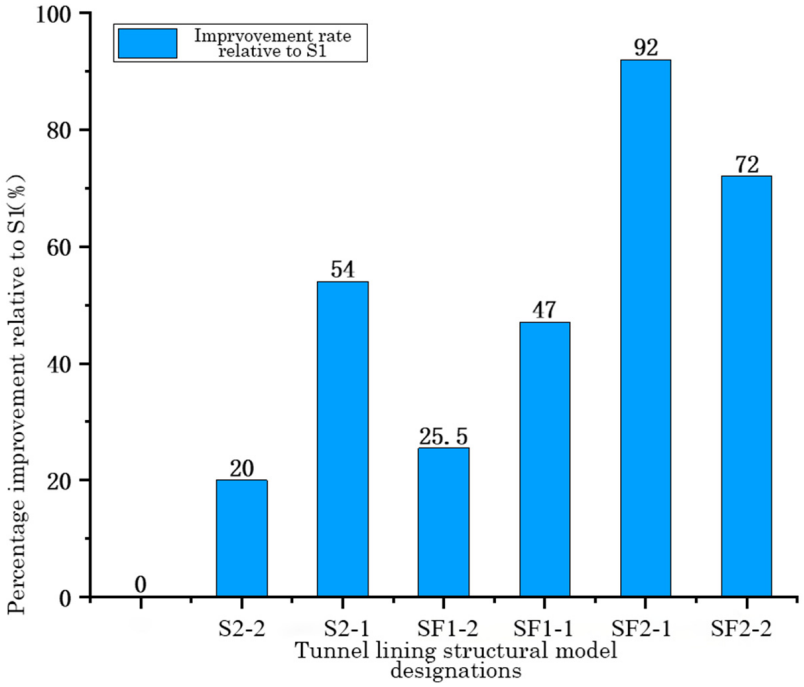


Figure 19. Percentage increase in bearing capacity relative to PC.

5. Analysis of Mechanical Behavior in the Optimal Tunnel Lining Structure

Analysis of the internal force evolution in structures can effectively reveal the stage-wise characteristics and governing indicators of the damage process, providing a theoretical basis for the design of SFRC tunnel linings. The axial force and bending moment of the lining section can be calculated from the strains measured on its inner and outer surfaces using Equations (2) and (3).

$$N = \sigma A = \frac{E\left(\varepsilon_{inner} + \varepsilon_{surface}\right)bh}{2} \tag{2}$$

$$M = \sigma W = \frac{E\left(\varepsilon_{inner} - \varepsilon_{surface}\right)bh^2}{12} \tag{3}$$

where N is the axial force of the section (KN), M is the bending moment of the section (KN.m), σ is the stress of the section (MPa), A is the cross-sectional area (m^2), W is the section modulus (m^3), E is the elastic modulus of the tunnel lining concrete (MPa), ε_{inner} is the strain on the inner surface of the tunnel lining, $\varepsilon_{surface}$ is the strain on the outer surface of the tunnel lining, b is the longitudinal unit length of the tunnel lining (m), and h is the thickness of the tunnel lining (m).

To further elucidate the internal force evolution of the hybrid steel bar and R/SFRC lining—previously identified as the optimal solution-and to establish a theoretical basis for engineering design, the internal forces developed during loading were analyzed for both unconditioned and freeze–thaw-exposed specimens. Strain data from the inner and outer surfaces at seven selected monitoring sections were obtained during testing. These data were substituted into Equations (2) and (3) to calculate the axial forces and bending moments at these sections throughout the loading process. The analysis focused on the variation patterns in key regions: the vault, haunch, and invert. The variations in internal forces with loading at these critical sections are presented in Figures 20 and 21.

Figure 20 illustrates the variation in axial forces at different sections of the tunnel lining under progressive vertical loading, comparing responses before and after F-T exposure. The results are as follows:

1. During the initial elastic stage, the axial force increased linearly with the vertical load. The first tensile cracks initiated at the inner side of the vault at vertical loads of approximately 24 KN (non-F-T) and 20 KN (F-T conditioned), respectively, inducing noticeable oscillations in the axial force curves.
2. With a further increase in load, a second tensile crack emerged in the right invert area, leading to a gradual transition in the axial force curves from linear to nonlinear. The subsequent formation of a third crack in the left haunch region indicated a shift in the primary cracking zone toward the haunch.
3. Continued loading prompted the formation of plastic hinges between the arch foot and the invert, which significantly altered and intensified the internal axial force distribution. The axial force rose sharply, peaking simultaneously in both the vault and arch foot regions, thereby identifying these as the critical zones governing structural performance. After the vertical load reached approximately 65 KN (non-F-T) and 55 KN (F-T conditioned), respectively, all lining sections entered the failure stage, marked by a definitive decrease in axial force indicating structural unloading and collapse.

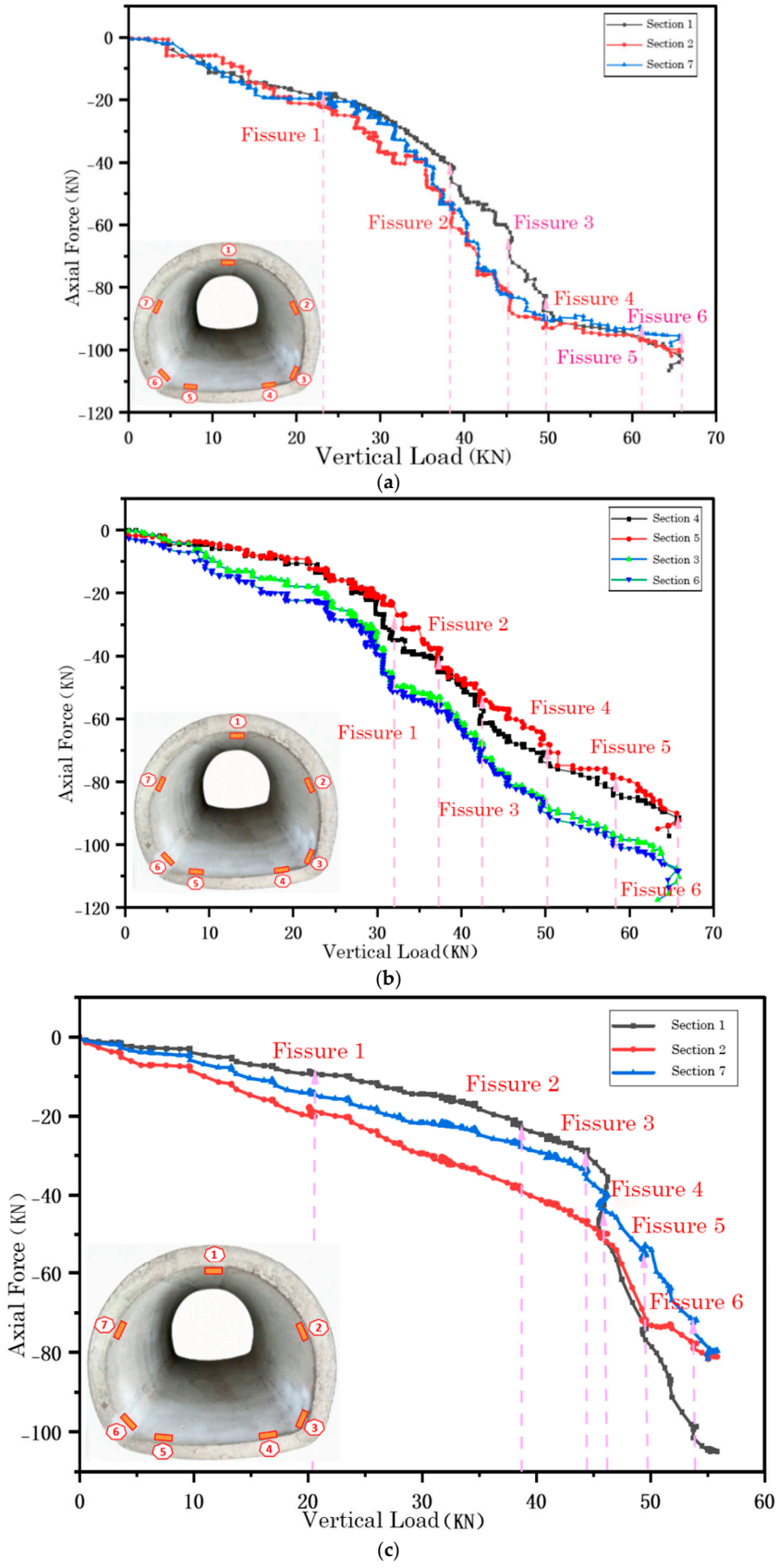


Figure 20. *Cont.*

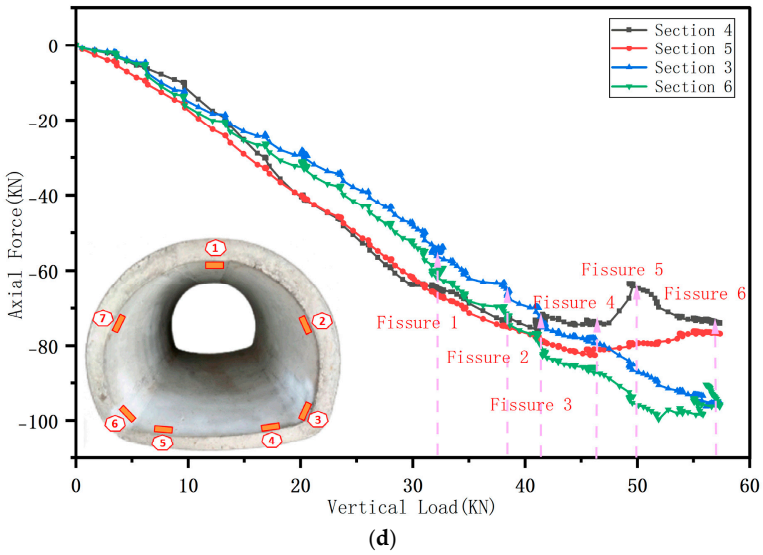
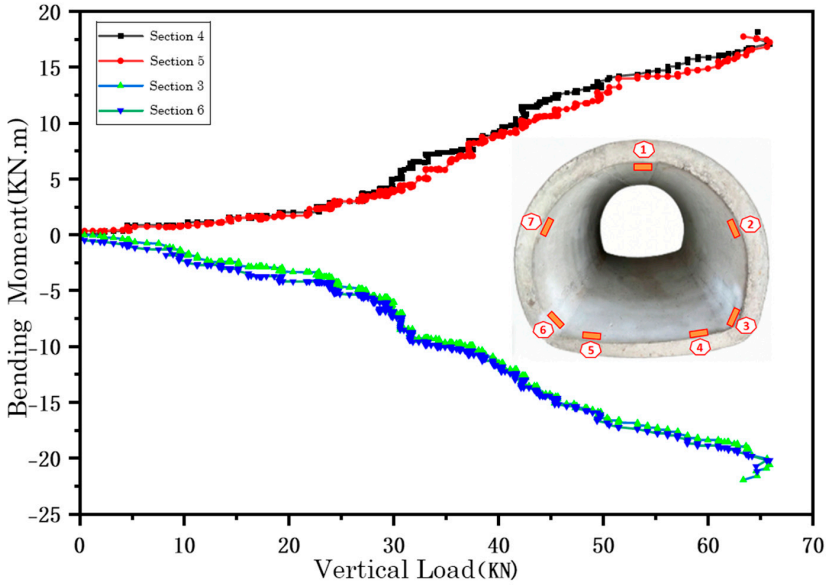


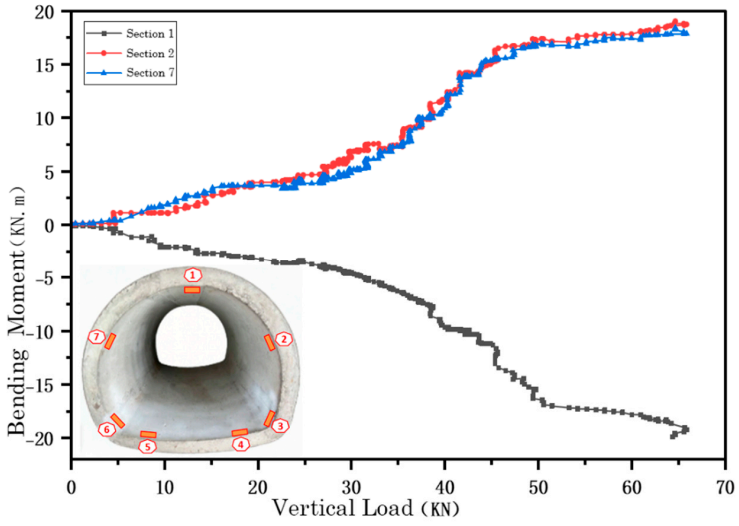
Figure 20. Axial forces at different sections of the tunnel lining before and after freeze–thaw exposure: (**a**) axial force at vault and haunch sections after 0 freeze–thaw cycles; (**b**) axial force at vault and haunch sections after 0 freeze–thaw cycles; (**c**) axial force at vault and haunch sections after 100 freeze–thaw cycles; (**d**) axial force at vault and haunch sections after 100 freeze–thaw cycles.

Figure 21 illustrates the variation in bending moments at critical sections of the tunnel lining under progressive vertical loading, comparing responses with and without prior F-T conditioning.

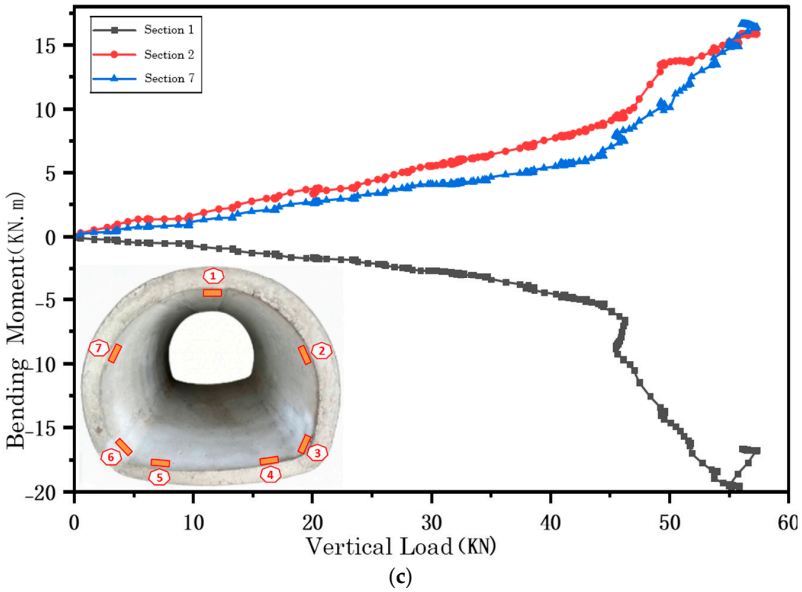
1. During the initial elastic stage, the bending moment increased linearly with the vertical load, indicating negligible structural damage. Upon reaching vertical loads of approximately 24 KN (non-F-T) and 20 KN (F-T conditioned), respectively, crack initiation at the vault triggered internal force redistribution, resulting in slight deviations from linearity in the bending moment curves.
2. The propagation of cracks led to a divergence in the bending moments developed at the invert, haunch, and arch foot sections. As illustrated, positive bending moments were recorded at the vault (Section 1) and invert (Sections 4 and 5), corresponding to compression on the outer face and tension on the inner face. Conversely, negative bending moments were observed at the haunch (Sections 2 and 7) and arch foot (Sections 3 and 6), indicating tension on the outer face and compression on the inner face.
3. With a further increase in load beyond approximately 45 KN (non-F-T), crack development intensified, particularly in the vault and invert regions. The bending moment curves exhibited significant oscillations at key sections, followed by a rapid increase as the load approached the ultimate state. Upon entering the failure stage, the overall growth rate of the bending moments slowed or declined, indicating that progressive cracking and the formation of plastic hinges reduced the structural stiffness and altered the internal force redistribution mechanism.



(a)

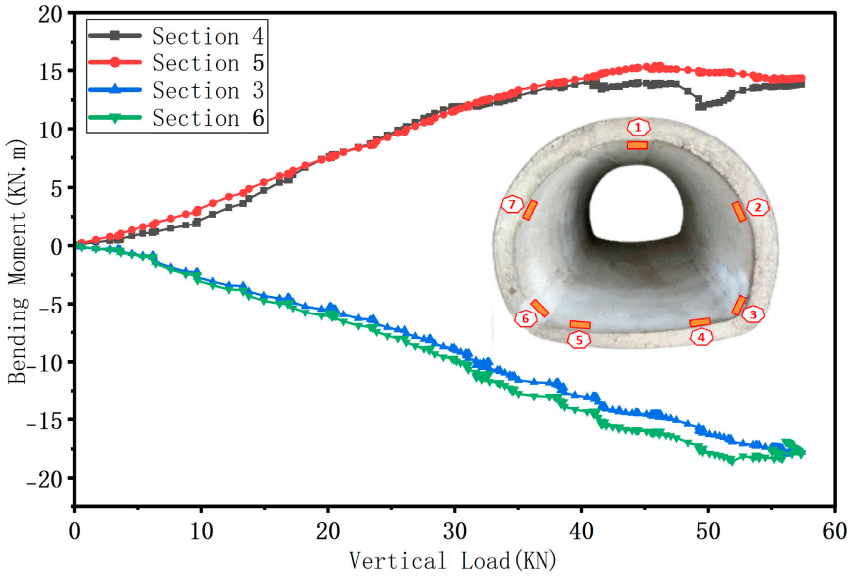


(b)



(c)

Figure 21. *Cont.*



(**d**)

Figure 21. Bending moments at different sections of the tunnel lining before and after freeze–thaw exposure: (**a**) bending moment at the vault and haunch sections before freeze–thaw exposure; (**b**) bending moment at the vault and haunch sections before freeze–thaw exposure; (**c**) bending moment at the vault and haunch sections after freeze–thaw exposure; (**d**) bending moment at the vault and haunch sections after freeze–thaw exposure.

A comparative analysis of the axial force and bending moment curves in Figures 20 and 21 for key lining sections under vertical loading, before and after F-T exposure, yielded the following insights:

1. During the initial loading stage, both the axial force and bending moment increased nearly proportionally with the applied load for both conditions, indicating a predominantly linear-elastic material response with negligible damage accumulation.
2. Throughout the entire loading history, the development of internal forces was more gradual and sustained significantly higher load levels in the non-F-T-conditioned lining compared to its F-T-exposed counterpart. This demonstrates that the freeze–thaw cycles notably increased material brittleness and reduced the structural ductility.
3. The observed mechanical behavior, coupled with the crack propagation patterns, indicates that the incorporation of steel fibers effectively delayed the sudden brittle fracture of the lining sections. This confirms that a suitable volume fraction of steel fibers can enhance structural ductility and suppress crack propagation in tunnel linings.

6. Conclusions

Systematic bearing-capacity tests were conducted on scaled tunnel lining models based on a cold-region tunnel project in Gansu Province, China. During testing, the applied load, along with strain and displacement data at key locations (vault, haunch, arch foot, and invert), was monitored in real time. Analysis of the data revealed the structural response and deformation patterns. The main conclusions are as follows:

1. The vault and arch foot were identified as the most vulnerable zones, being the first to exhibit cracks of varying severity. The stress state at the arch foot was particularly complex, leading to pronounced crack propagation, typically in a triangular pattern, and resulting in severe damage.
2. Compared to the non-freeze–thaw (F-T)-conditioned specimens, F-T cycles increased the brittleness and reduced the ultimate bearing capacity of the lining. Although the

addition of steel fibers improved overall ductility, crack propagation still occurred through the concrete matrix between the fibers. All steel-reinforced models demonstrated significantly higher bearing capacity and ductility than their unreinforced counterparts. Compared to non-freeze–thaw SFRC (SF1-2), the load-bearing capacity of freeze–thaw-cycled R/SFRC (SF2-2) increased by approximately 37.4%.

3. Under the specific reinforcement ratio and steel fiber volume fraction conditions adopted in this test, the load-bearing capacity of reinforced concrete was 4.2% lower than that of plain steel fiber-reinforced concrete, indicating that steel fiber-reinforced concrete structures can serve as a viable alternative to traditional reinforced concrete structures at certain fiber volume fractions. Furthermore, the fiber-reinforced specimens exhibited superior freeze–thaw resistance and enhanced crack resistance, thereby improving the relative ductility of the structure under freeze–thaw conditions.

Author Contributions: Conceptualization, L.-M.W. and F.G.; methodology, L.-M.W. and Z.-J.W.; software, L.-M.W.; validation, L.-M.W.; formal analysis, L.-M.W.; investigation, L.-M.W. and H.-X.-T.H.; resources, L.-M.W., F.G. and Z.-J.W.; data curation, L.-M.W.; writing—original draft preparation, L.-S.L.; writing—review and editing, L.-M.W. and Z.-J.W.; visualization, L.-M.W.; supervision, L.-M.W. and Z.-J.W.; project administration, Z.-J.W. and W.-J.L.; funding acquisition, L.-M.W. All authors have read and agreed to the published version of the manuscript.

Funding: This research was supported by the Science and Technology Research Program of Chongqing Municipal Education Commission (Grant No. KJZD-K202504002). The APC was funded by 202504002.

Institutional Review Board Statement: Not applicable.

Informed Consent Statement: Not applicable.

Data Availability Statement: The original contributions presented in this study are included in the article. Further inquiries can be directed to the corresponding authors.

Acknowledgments: The successful completion of this study would not have been possible without the generous assistance of many institutions and individuals. We would like to thank Lin Zhi's team from Chongqing Jiaotong University for their professional technical support with the reaction frame equipment used to simulate confining pressure. We are also grateful to Wang Zijian's team at Chongqing University of Science and Technology for their assistance with the experiments. Additionally, we acknowledge the laboratory at Chongqing Jiaotong University for the convenience and assistance provided in project coordination and administrative affairs. The authors have reviewed and edited the generated content and take full responsibility for the final version of this publication.

Conflicts of Interest: The authors declare no conflict of interest.

References

1. Mehta, P.K. Concrete durability-fifty years progress. In Proceedings of the 2nd International Conference on Concrete Durability, Montreal, QC, Canada, 1 September 1991; p. 132.
2. Wen, C.M. Simulate Initiation and Formation of Cracks and Potholes. Master's Thesis, Northeastern University, Boston, MA, USA, 2016.
3. Guler, S.; Akbulut, Z.F. Effect of freeze-thaw cycles on strength and toughness properties of new generation 3D/4D/5D steel fiber-reinforced concrete. *J. Build. Eng.* **2022**, *51*, 104239. [CrossRef]
4. Cai, D.; Luo, L.; Zhu, K.; Lu, F. Performance Deterioration of Lining Structure of Cold Region Tunnels Under Freeze-thaw Cycles. *Railw. Stand. Des.* **2026**, 1–11. [CrossRef]
5. Sun, K.G.; Jia, J.L.; Feng, K.; Xu, W.P.; Zhang, H.J. Experimental design of a coupled hydro-thermal-mechanical loading model for tunnel lining components in cold regions. *Exp. Technol. Manag.* **2025**, *42*, 10–18. [CrossRef]
6. Xia, C.C.; Huang, W.F.; Han, C.L. A study of the service performance of tunnel lining in the cold zone when subjected to the freeze-thaw cycle. *J. Harbin Eng. Univ.* **2020**, *41*, 347–356.

7. Arora, S.; Singh, S.P. Fatigue strength and failure probability of concrete made with RCA. *Mag. Concr. Res.* **2016**, *69*, 55–67. [CrossRef]
8. Bernal, S.A.; Mejía de Gutiérrez, R.; Provis, J.L. Engineering and durability properties of concretes based on alkali-activated granulated blast furnace slag/metakaolin blends. *Constr. Build. Mater.* **2012**, *33*, 99–108. [CrossRef]
9. Singh, A.; Kumar, R.; Mehta, P.K.; Tripathi, D. Effect of nitric acid on Rice Husk Ash steel fiber reinforced concrete. *Mater. Today Proc.* **2020**, *27*, 995–1000. [CrossRef]
10. Zhou, T.; Xiong, X.B.; Li, Y. Influence of freeze—Thaw cycles on dynamic performance of steel fiber reinforced concrete. *J. Water Resour. Water Eng.* **2021**, *32*, 167–172+178.
11. Zhang, G.T.; Liu, S.T.; Geng, T.J.; Pen, R.; Chen, Y. On damage model of fiber concrete based on the Weibull distribution in freezing-thawing cycle. *Sci. Technol. Eng.* **2020**, *20*, 12078–12084.
12. Shi, J.W.; Song, Z.P.; Cui, G.J.; Cheng, Y.; Yan, B. Study on frost resistance of steel fiber gangue concrete under freeze-thaw cycles. *J. Xi'an Univ. Archit. Technol. (Nat. Sci. Ed.)* **2023**, *55*, 52–59. [CrossRef]
13. Zhang, Z.J.; Yao, Z.Q.; Ma, K.L. Frost resistance life of steel–basalt fiber reinforced concrete based on multiple regression model. *J. Drain. Irrig. Mach. Eng.* **2025**, *43*, 819–825.
14. Zhang, H.; Liu, X.; Bai, L.; Ji, S.; Pan, L.; Li, X. Acoustic emissions evaluation of the dynamic splitting tensile properties of steel fiber reinforced concrete under freeze–thaw cycling. *Front. Struct. Civ. Eng.* **2023**, *17*, 1341–1356. [CrossRef]
15. Zeng, W.; Ding, Y.; Zhang, Y.; Dehn, F. Effect of steel fiber on the crack permeability evolution and crack surface topography of concrete subjected to freeze-thaw damage. *Cem. Concr. Res.* **2020**, *138*, 106230. [CrossRef]
16. Li, J.Y.; Zhu, Y.P.; Luo, J.W.; Fan, X.M.; Wang, X.Y.; Chen, L.; Zhang, Z.C. Experimental study on frost resistance of steel fiber reinforced concrete. *J. Phys. Conf. Ser.* **2024**, *2808*, 012028. [CrossRef]
17. Pan, K.; Ma, C.; Yu, R.C.; Wu, Z. Multi-index evaluation of steel fiber's crack resistance enhancement in desert sand concrete under freeze-thaw cycles: Optimization, fracture, and mechanism. *Constr. Build. Mater.* **2025**, *499*, 144059. [CrossRef]
18. Li, D.; Guo, Q.; Liu, S. Influence of Steel Fiber on Durability Performance of Concrete under Freeze-Thaw Cycles. *Adv. Mater. Sci. Eng.* **2021**, *2021*, 5460844. [CrossRef]
19. Nili, M.; Azarioon, A.; Danesh, A.; Deihimi, A. Experimental study and modeling of fiber volume effects on frost resistance of fiber reinforced concrete. *Int. J. Civ. Eng.* **2018**, *16*, 263–272. [CrossRef]
20. Zhang, Q.Y.; Xu, W.W.; Sun, Y.C.; Ji, Y.C. Investigation on Mechanical and Microstructure Properties of Steel Fiber Reinforced Concrete. *Adv. Mater. Sci. Eng.* **2022**, *2022*, 3681132. [CrossRef]
21. Niu, D.T.; Jiang, L.; Bai, M.; Miao, Y.Y. Study of the performance of steel fiber reinforced concrete to water and salt freezing condition. *Mater. Des. (1980–2015)* **2013**, *44*, 267–273. [CrossRef]
22. *JTG/T 3370.1-2018*; Specifications for Design of Highway Tunnels—Section 1: Civil Engineering. Ministry of Transport: Beijing, China, 2018.
23. *GB/T 50082-2009*; Standard for Test Methods of Long-Term Performance and Durability of Ordinary Concrete. National Standard of the People's Republic of China: Beijing, China, 2009.
24. Cao, X.P.; Zhang, Y.P.; Wei, Z.K.; Li, T.; Liang, Q.G. Analysis on Surrounding Rock Pressure during Construction of Shallow Buried Bias Loess Tunnel with Small Clear Distance. *Chin. J. Undergr. Space Eng.* **2023**, *19*, 1422–1432+1443. [CrossRef]

Disclaimer/Publisher's Note: The statements, opinions and data contained in all publications are solely those of the individual author(s) and contributor(s) and not of MDPI and/or the editor(s). MDPI and/or the editor(s) disclaim responsibility for any injury to people or property resulting from any ideas, methods, instructions or products referred to in the content.